Wiley Analytical Science

Virtual Conference

The 5th edition of the Wiley Analytical Science Conference starts November 8, 2022!

Featured Sessions:

- **Integration of X-ray microscopy and finite elements into a digital twin**

  Thurs Nov 10, 10:00 - 10:30 AM EST / 4:00 - 4:30 PM CET

- **Optimization of Cryo TEM lamella preparation workflows to be faster and more accessible**

  Wed Nov 16, 10:00 - 11:00 AM EST / 4:00 - 5:00 PM CET

events.bizzabo.com/WASconferenceFall2022

ZEISS
Seeing beyond

TESCAN
PERFORMANCE IN NANOSPACE

WILEY

ADVANCED
MATERIALS

www.advmat.de

Turbostratic Boron–Carbon–Nitrogen and Boron Nitride by Flash Joule Heating

Weiyin Chen, John Tianci Li, Chang Ge, Zhe Yuan, Wala A. Algozeeb, Paul A. Advincula, Guanhui Gao, Jinhang Chen, Kexin Ling, Chi Hun Choi, Emily A. McHugh, Kevin M. Wyss, Duy Xuan Luong, Zhe Wang, Yimo Han, and James M. Tour*

Turbostratic layers in 2D materials have an interlayer misalignment. The lack of alignment expands the intrinsic interlayer distances and weakens the optical and electronic interactions between adjacent layers. This introduces properties distinct from those structures with well-aligned lattices and strong coupling interactions. However, direct and rapid synthesis of turbostratic materials remains a challenge owing to their thermodynamically metastable properties. Here, a flash Joule heating (FJH) method to achieve bulk synthesis of boron–carbon–nitrogen ternary compounds with turbostratic structures by a kinetically controlled ultrafast cooling process that takes place within milliseconds (10^3 to 10^4 K s^{-1}) is reported. Theoretical calculations support the existence of turbostratic structures and provide estimates of the energy barriers with respect to conversion into the corresponding well-aligned counterparts. When using non-carbon conductive additives, a direct synthesis of boron nitride is possible. The turbostratic nature facilitates mechanical exfoliation and more stable dispersions. Accordingly, the addition of flash products to a poly(vinyl alcohol) nanocomposite film coating a copper surface greatly improves the copper's resistance to corrosion in 0.5 M sulfuric acid or 3.5 wt% saline solution. FJH allows the use of bulk materials as reactants and provides a rapid approach to large quantities of the hitherto hard-to-access turbostratic materials.

1. Introduction

Canonical layered materials usually have a distinct and thermodynamically favored stacking sequence under standard temperature and pressure conditions.[1,2] The stacking sequence is determined by various noncovalent interactions, such as London and Keesom interactions.[3] Deviation from these stacking morphologies leads to the formation of turbostratic lattices with the expansion of intrinsic interlayer distances and the weakening of coupling interactions between the neighboring layers,[4,5] which can introduce unique optical, electrical, and magnetic properties for turbostratic materials, thus broadening their applications.[6,7]

A major concern for the synthesis of turbostratic materials lies in the unfavorable formation energy and the spontaneous relaxation towards the thermodynamically favored stacking sequence. Once a sustained heat source is provided, products with thermodynamically most stable layered sequences dominate, making the access to turbostratic structures difficult.[2,8–10] Therefore, most bottom-up methods for preparing layered materials cannot be adopted for synthesizing turbostratic materials because of an insufficient relaxation energy barrier (<4 kJ mol^{-1})[11] and limited cooling rate (<10 K s^{-1}).[12,13] The organization of regular in-plane configurations is usually accompanied by the formation of self-limited monolayer or well-aligned multilayer structures. Although previous work has demonstrated that the formation of turbostratic structures can be induced by low-temperature (≈500 K) heat treatment, or bias-assisted hot-filament chemical vapor deposition (CVD), these products usually have a semicrystalline in-plane configuration with hybrid nanocrystalline and amorphous domains.[14,15] The semicrystalline in-plane structures can prevent the precise stacking of individual layers, which induces the formation of the turbostratic stacking structures. In addition, guest intercalation methods using ionic liquids[16] and chemical functionalization[17] have been used to stabilize turbostratic materials. These methods are ascribed to the modification of interlayer interactions, such as hydrogen bonds and π–π stacking between neighboring basal planes. Therefore, the

W. Chen, J. T. Li, C. Ge, Z. Yuan, W. A. Algozeeb, P. A. Advincula, J. Chen, K. Ling, E. A. McHugh, K. M. Wyss, D. X. Luong, Z. Wang, J. M. Tour
Chemistry Department
Rice University
6100 Main Street MS 60, Houston, TX 77005, USA
E-mail: tour@rice.edu
C. Ge, D. X. Luong
Applied Physics Program
Rice University
6100 Main Street MS 60, Houston, TX 77005, USA
G. Gao, C. H. Choi, Y. Han, J. M. Tour
Department of Materials Science and NanoEngineering
Rice University
6100 Main Street, Houston, TX 77005, USA
J. M. Tour
NanoCarbon Center and the Welch Institute for Advanced Materials
Smalley-Curl Institute
Rice University
6100 Main Street MS 222, Houston, TX 77005, USA

The ORCID identification number(s) for the author(s) of this article can be found under https://doi.org/10.1002/adma.202202666.

ADVANCED
SCIENCE NEWS
www.advancedsciencenews.com

ADVANCED
MATERIALS
www.advmat.de

direct synthesis of turbostratic materials with high in-plane crystallinity remains challenging when one wants to study the unique properties caused by the weak coupling effect between neighboring layers.

The semicrystalline in-plane structure is common for multicomponent systems when starting from gaseous precursors, such as boron–nitrogen dual compounds[18] and boron–carbon–nitrogen ternary compounds (BCN).[15,19] These reactive precursors, such as BCl_3 and NH_3,[19] or ammonia borane (BH_3NH_3),[20] achieve fast conversion and cause the formation of amorphous products with numerous structural imperfections. Although the in-plane crystallinity of the products can be improved by controlling the annealing time and temperature, either semicrystalline structures or well-aligned stacking structures eventually form[12,15] because of the thermodynamic limitation of these traditional bottom-up methods and metastable features of turbostratic materials with high in-plane crystallinity.[1,2] Hexagonal boron nitride (h-BN) and graphene are two common layered materials whose interlayer interactions are ≈26 meV atom^{-1} (≈2.5 kJ mol^{-1}),[11] while the in-plane binding energy is ≈450 kJ mol^{-1}, more than two orders of magnitude higher than the interlayer interactions. Therefore, the formation of turbostratic materials with high in-plane crystallinity can be kinetically controlled by a thermal annealing followed by an ultrafast cooling process.[1,2] The thermal annealing facilitates the formation of ordered in-plane structures,[2] and the ultrafast cooling process preserves the misaligned stacking sequences in local, rather than global energy minima. This can be extended to doped graphene as well.[21]

Here, we report a scalable bottom-up method to synthesize BCN with turbostratic structures and high in-plane crystallinity via an all-solid-state flash Joule heating (FJH) system.[1,22–24] It provides short pulses of high electrical energy followed by rapid cooling (10^3–10^4 K s^{-1}), all in <1 s. Starting from BH_3NH_3 and carbon black, the FJH-product is named flash BCN (f-BCN-x, where x is the carbon percentage in the reactants). Other conductive powder additives, such as iron and tungsten can also be used to replace the carbon black, and in this case, carbon-free flash BN (f-BN can be prepared). The atomic percentage of carbon can be controlled from $\approx0\%$ to $\approx100\%$ as determined via X-ray photoelectron spectroscopy (XPS) by changing or eliminating the carbon content in the reactants. At the lower percentage of carbon or at 0% carbon additive, closely aligned spectroscopic features to those of pure turbostratic h-BN (t-BN) are observed. The f-BCN has a turbostratic arrangement, which facilitates its exfoliation by different mechanical methods, such as adhesive tape exfoliation, monodirectional mechanical shearing, and bath sonication. Theoretical calculation results support the existence of turbostratic structures and the energy barriers converting to well-aligned counterparts. Compared to commercial h-BN and graphene, f-BCN has better temporal stability when dispersed in aqueous Pluronic (F-127, 1 wt% in deionized water). Polyvinyl alcohol (PVA) nanocomposites containing 10 wt% f-BCN that are coated on copper foils confer improved corrosion resistance when subjected to 0.5 M sulfuric acid or 3.5 wt% saline solution. FJH offers access to bulk quantities of BCN with turbostratic structures for further fundamental research and broad varieties of applications.

2. Results and Discussion

2.1. All-Solid-State Synthesis of f-BCN by FJH

Figure 1a illustrates the ultrafast all-solid-state preparation process based on FJH to synthesize the f-BCN in <1 s. In a typical flash process,[25] a mixture of BH_3NH_3 and commercial carbon black is slightly compressed inside a quartz tube between two copper electrodes. BH_3NH_3 is chosen as the reactant as it serves as both a boron and nitrogen source, and there are preformed B−N bonds in the precursor. Carbon black simultaneously acts as the carbon source and the conductive agent during the reaction. The capacitor banks in the circuit are used to provide electrothermal energy to the reactants (Figure S1, Supporting Information). By changing the carbon content in the mixture, the FJH process can be used to synthesize f-BCN with various compositions and turbostratic structures. During a typical flash reaction with a voltage of 150 V and a sample resistance of ≈40 Ω, the current passing through the sample reaches ≈15 A in ≈600 ms discharge time (Figure S1, Supporting Information). The total amount of electrical energy is 3.1 kJ g^{-1} and the energy cost for converting 1-ton BH_3NH_3 precursor into flash product is $\approx\$19$ (Note S1, Supporting Information). The real-time temperature can be measured using an infrared sensor as plotted in Figure 1b. The temperature reaches ≈1220 K within ≈600 ms with a ramp rate in the heating stage that is estimated to be ≈1300 K s^{-1}, followed by rapid cooling at ≈1600 K s^{-1}. Other carbon-free conductive additives, such as tungsten and iron, are also tried, and the flash products are named f-BN-W and f-BN-Fe, respectively. Specifically, iron powder can be collected by a magnet and reused (Figure S2, Supporting Information). The formation of BN without obvious carbon signal is shown in Figure S3 (Supporting Information). Due to the possible catalytic effect of Cu during the reaction, graphite spacers are used as the alternatives of the Cu wool plugs. To facilitate the outgassing and avoid the explosion of the tube, the diameter of the graphite spacer is ≈1 mm smaller than the quartz tube. The formation of the BN is shown in Figure S4 (Supporting Information).

Previous pyrolytic dehydrogenation analysis has reported that there are three thermal decomposition steps to form BN-based structures from the BH_3NH_3 precursor,[26] and that the overall reaction is highly exothermic (-171 kJ mol^{-1}). This drives the reaction to completion, even though the third step, dehydrogenation, NHBH(s) to BN(s), has a high kinetic barrier and generally requires a higher temperature of 1200–1400 K (Note S2, Supporting Information).[18,26] Compared to other bottom-up methods, such as CVD[10,27] and hydrothermal methods,[28,29] which usually involve a much slower cooling rate of <10 K s^{-1} and result in the formation of well-aligned stacking morphologies, the FJH method has a 100–1000× faster cooling rate and generates turbostratic BCN (t-BCN) as shown in Figure 1c. Simulations are performed using the finite element method (FEM), and the temperatures reached in the bulk of the sample are found to be sufficient for driving the third decomposition step since the timescale of the uniform energy input is relatively short compared to that of heat diffusion (Figures S5 and S6, Supporting Information). An
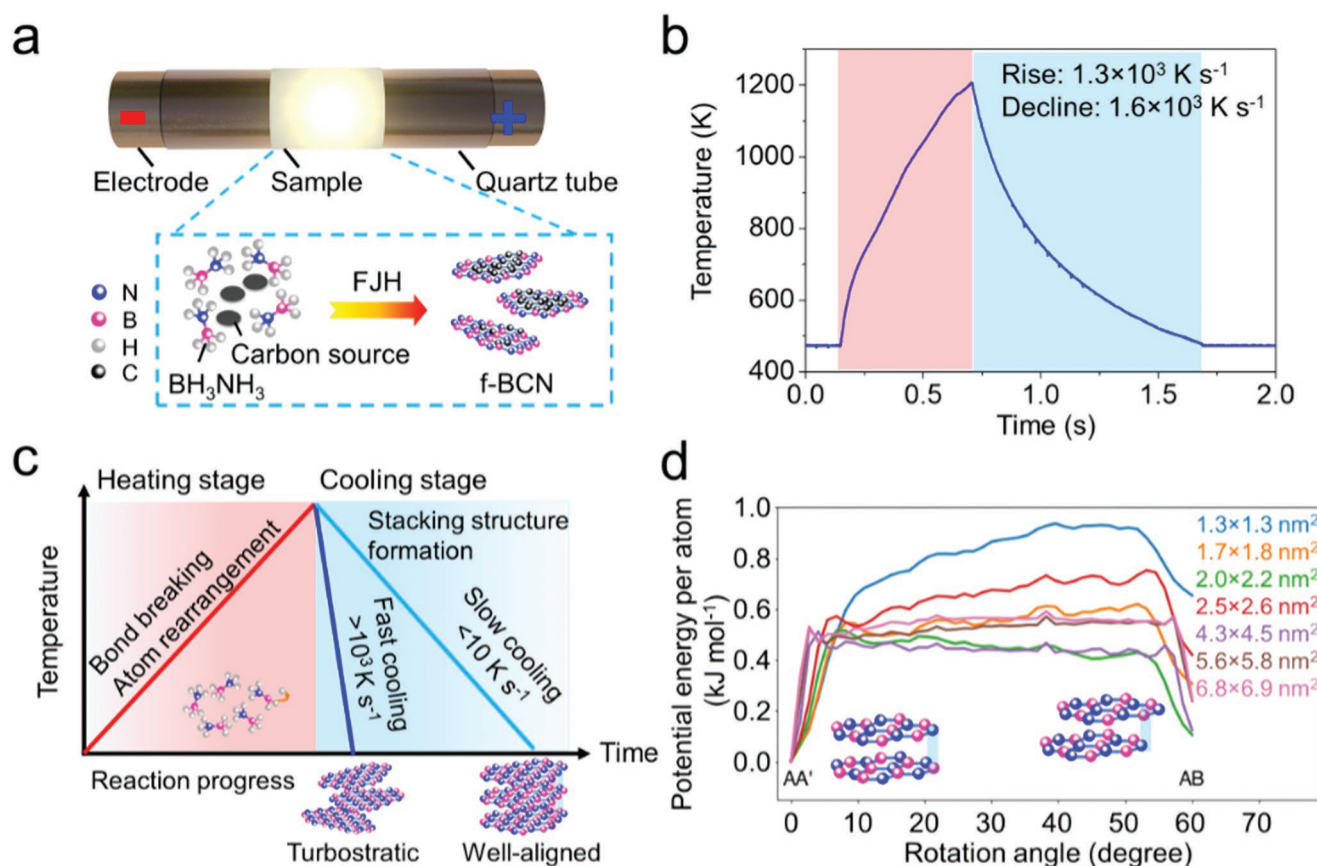
Figure 1. All-solid-state synthesis of f-BCN by flash Joule heating. a) Schematic diagram for the formation of f-BCN from BH_3NH_3 and carbon via FJH. b) The real-time temperature measurement from the sample during the FJH process. c) Time–temperature transformation diagram showing the kinetic formation of the turbostratic structure with ultrafast cooling ($>10^3$ K s^{-1}). d) The potential energy profiles of h-BN sheets of various sizes (per atom) along the rotational minimum energy pathways from AA′ to AB stacking.

animation of the simulated temperature distribution during the flash process is included (Video S1, Supporting Information).

Nudged elastic band (NEB) simulations are performed to study the thermodynamic stability against in-plane rotation by using h-BN as an example (Figure S7, Supporting Information). Figure 1d shows the potential energy profiles of h-BN sheets with different sizes along the rotational minimum energy pathways from AA′- to AB-stacking. All potential energies are normalized by the total number of atoms in the small h-BN sheets and are relative to the most stable AA′ stacking mode. The calculations indicate that: (1) t-BN is generally ≈0.5 kJ mol^{-1} higher in energy than AA′-stacked h-BN. The energy difference may be larger when the h-BN sheet is very small; (2) except for the smallest h-BN sheet (1.3 × 1.3 nm^2), all other energy profiles exhibit an energy barrier realigning from turbostratic (rotation angle ≠ 0° or 60°) stacking to AA′- or AB-stacking. This energy barrier of realignment accounts for t-BN's is metastability; (3) the slope of the energy profile near 0° is steeper for larger h-BN sheets. This results because a larger h-BN sheet has a higher chance of interlayer misalignment (e.g., N on top of N or B on top of B, leading to large electrostatic repulsion), even when the rotation angle is small. The energy barrier of realignment per atom is nearly size-independent (≈0.054 kJ mol^{-1} = 0.56 eV

to AA′, and ≈0.039 kJ mol^{-1} = 0.40 eV to AB) as listed in Table S1 (Supporting Information). Therefore, the formation of BN-based turbostratic structure is kinetically possible, which can be achieved by the FJH method with the ultrafast heating and cooling process.

2.2. Spectroscopic Analysis and Crystal Structure of f-BN

When a mixture of BH_3NH_3 and 20 wt% carbon black is used as the reactant, the flash product shows similar spectroscopic features as h-BN. Therefore, f-BCN-20 is also called flash BN (f-BN) in this context. BH_3NH_3 and f-BN can be analyzed by Fourier-transform infrared spectroscopy (FTIR); it is noted that there are no interfering peaks of carbon black or flash graphene (FG)[1] in the IR spectra (Figure S8, Supporting Information). There is no obvious N-H or B-H stretching band in the f-BN product as shown in **Figure 2**a, which indicates the complete conversion of BH_3NH_3.[26] The f-BN product shows a B−N stretching peak (E_{1u} mode, ≈1353 cm^{-1}) and a B−N−B bending peak (A_{2u} mode, ≈782 cm^{-1})[30] in the IR spectrum, which is similar to the spectrum of commercial h-BN. The shoulder peak at ≈1074 cm^{-1} is ascribed to the B−C band. FTIR result
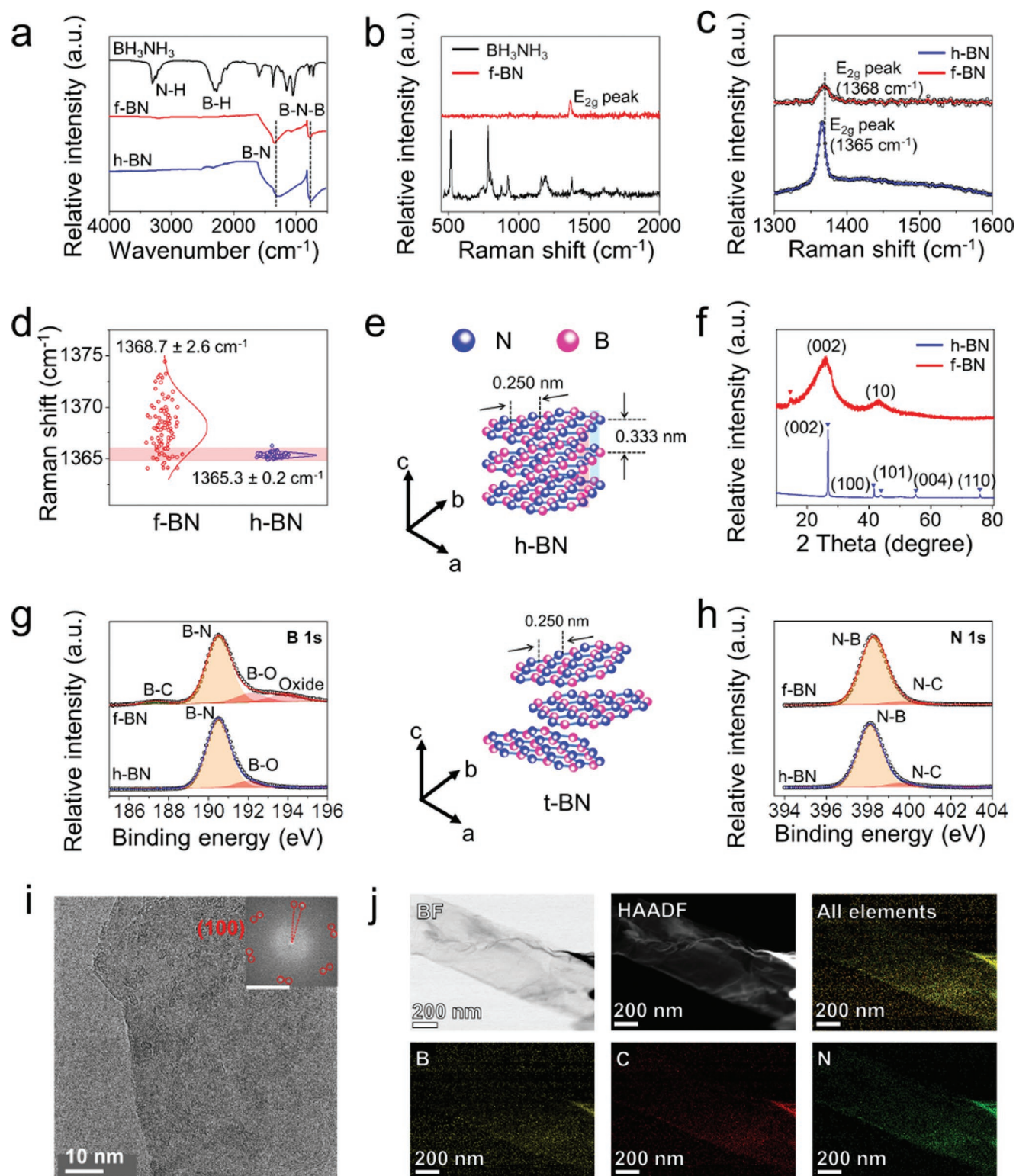
Figure 2. Spectroscopic analysis and crystal structure of f-BN. a) FTIR spectra of BH_3NH_3 (black), f-BN (red), and commercial h-BN (blue). b) Raman spectra of BH_3NH_3 and f-BN. c) Representative high-resolution Raman spectra reporting E_{2g} peak positions of f-BN and commercial h-BN. d) The statistic survey about E_{2g} peak positions of f-BN and commercial h-BN. Number of samples $N = 100$. e) A scheme showing the structures of h-BN and t-BN. f) XRD spectra of f-BN and commercial h-BN. g,h) High-resolution XPS spectra of commercial h-BN and f-BN: g) B 1s and h) N 1s spectra. i) HRTEM images of f-BN sheets. The inset shows the FFT patterns, and the scale bar is 5 nm^{-1}. j) BF-STEM, HAADF-STEM images, and corresponding elemental distribution of f-BN sheets.

**ADVANCED
SCIENCE NEWS**

www.advancedsciencenews.com

**ADVANCED
MATERIALS**

www.advmat.de

is consistent with the Raman spectra in Figure 2b. There are many Raman peaks for BH_3NH_3 between 500 and 1200 cm^{-1}, whereas these peaks are absent in f-BN and the characteristic E_{2g} peak appears (Figure 2b). Compared to bulk h-BN, the E_{2g} peak in the Raman spectrum shows a blueshift as the number of layers decreases and there is an ≈4 cm^{-1} blueshift in isolated monolayer h-BN due to the shorter BN bonds and the hardening of E_{2g} mode.[31,32] From representative high-resolution Raman spectra shown in Figure 2c, there is an ≈3 cm^{-1} blueshift of the characteristic E_{2g} peak and a lower integrated intensity $I(E_{2g})$ for the f-BN, which resembles features of few-layer h-BN sheets and indicates the weakened coupling interaction between adjacent layers.[31] The E_{2g} peak positions of 100 different spots on f-BN and h-BN are studied in Figure 2d. Commercial h-BN belongs to bulk h-BN, whose E_{2g} peaks are centered at 1365.3 cm^{-1} with a narrow distribution (≈0.2 cm^{-1}, red shadow region). The f-BN has a higher average E_{2g} peak (≈1368.7 cm^{-1}) with a broader distribution (≈2.6 cm^{-1}), and ≈72% of the region shows a blueshift of the E_{2g} peak, which indicates the prevailing decoupling effect in the f-BN sample.

The scheme in Figure 2e displays a normal in-plane lattice constant ≈0.25 nm and interlayer spacing ≈0.33 nm in well-aligned h-BN crystals. There are random translational and rotational orientations of individual sheets in t-BN crystals with larger average interlayer distances. The turbostatic nature of the f-BN sample is further explored by X-ray diffraction (XRD) in Figure 2f. The (002) diffraction peak becomes broader but less intense and shifts toward a lower angle from ≈26.7° to 26.1°, indicating the expansion of the interlayer spacing by ≈2.3%. The (100) and (101) peaks merge into a broad (10) peak in f-BN and the long-range order diffraction peaks, such as (110) and (004), are absent. These results support the absence of an ordered structure of basal planes, and the existence of a turbostatic structure.[33–35] Elemental analyses carried out by XPS indicate the atomic ratio of B to N is ≈1.05 and the existence of 6.7 at% C (Figure S9 and Table S2, Supporting Information). High-resolution B 1s and N 1s spectra indicate the dominance of typical B—N bonds (≈190.5 eV) and N—B bonds (≈398.2 eV) (Figure 2g,h).[8,36] A small B—C peak (≈187.3 eV) is observed, which is consistent with the B—C band as shown in FTIR. The valence band of f-BN shows the valence band maximum (VBM) is −3.10 eV (Figure S9c, Supporting Information), which slightly downshifts compared with that of commercial h-BN (−2.70 eV). Ultraviolet–visible (UV–vis) spectra of commercial h-BN and f-BN indicate the optical bandgap of ≈6.0 eV (Figure S10, Supporting Information).[8] The Brunauer–Emmett–Teller (BET) method shows that the specific surface area of f-BN (≈143 m^2 g^{-1}) is ≈7-fold larger than that of commercial h-BN (≈22 m^2 g^{-1}), as shown in Figure S11 (Supporting Information). The larger surface area of f-BN is likely the result of small flake sizes and average layer numbers. The larger nanopore size distribution can come from the gaps between the small flakes. Conversely, the commercial h-BN samples are composed of thick microplates with >10 layers and well-aligned structure.

The f-BN sheets can reach up to ≈4.3 μm in lateral size with a wrinkled structure (Figure S12, Supporting Information). High-resolution transmission electron microscopy (HRTEM) analysis shows two stacking f-BN layers. Corresponding fast

Fourier transform (FFT) patterns indicate the existence of two sets of sixfold diffraction patterns close to each other with a rotational mismatch of ≈12°, which results from the turbostatic structure of the f-BN (Figure 2i). Polycrystalline materials are composed of many crystalline domains with various sizes and orientations, which give multiple sets of diffraction patterns. To identify the turbostatic structure (Figure S13 and Note S3, Supporting Information),[37,38] top-view atomic HRTEM images are taken as shown in Figure S14 (Supporting Information). The in-plane Moiré patterns are observed from the few layers areas. The clear edge fringes and FFT patterns indicate good crystallinity of the flash sample. The FFT patterns are compared at different positions atop the same sheets (Figure S15, Supporting Information). Due to the unchanged orientations and spot numbers of the diffraction spots, the possibility of polycrystals in this area is excluded. Therefore, the various sets of diffraction spots result from the turbostatic structure. The bright-field (BF) and high-angle annular dark-field scanning transmission electron microscopy (HAADF-STEM) images, together with elemental mapping, indicate the existence of B, N, and a small amount of C in f-BN sheets (Figure 2j), which is consistent with the XPS results. Plate-like f-BN with lateral sizes of 20–50 nm can also be observed (Figure S16, Supporting Information). HRTEM images show the crystallinity of f-BN nanoplates with the majority of these nanoplates only several layers thick. Corresponding FFT images show there are at least three sets of sixfold diffraction patterns. The estimated mass yield of f-BN is ≈34%. The conductive carbon additive can be removed from f-BN by thermal treatment under air (Figure S17, Supporting Information). However, oxidation will occur simultaneously on the surface (Figure S18 and Table S3, Supporting Information). There are small amounts of B—C and B—O bonds in f-BN, which is reasonable since previous studies have shown that the oxidation of B—C bonds starts at ≈600 °C.[36,39]

2.3. Mechanical Exfoliation Tests of f-BN

The turbostatic characteristics of f-BN facilitate its exfoliation by various mechanical methods, such as adhesive tape exfoliation, monodirectional mechanical shearing, and bath sonication (Table S4, Supporting Information). Few-layer f-BN sheets obtained by adhesive tape exfoliation can be distinguished from top-view scanning electron microscopy (SEM) as shown in **Figure 3**a. In contrast, due to the strong coupling between adjacent layers in commercial h-BN, there is no obvious exfoliation and only thick nanoplates of several hundred nanometers are observed in Figure 3b. The average lateral size of f-BN and commercial h-BN, obtained from the tape exfoliation method, are 0.40 and 0.34 μm, respectively (Figure 3c). The size distribution results show that the majority of the f-BN flakes have the lateral size no more than 1.0 μm, which makes it difficult to be applied in electronic devices, such as field-effect transistors.[40] However, the merits of f-BN, such as the nanoscale feature and good dispersibility (Figure S19, Supporting Information), show the potential applications of f-BN as the nanofillers to enhance the mechanical properties and to improve the electrochemical anticorrosion performance as
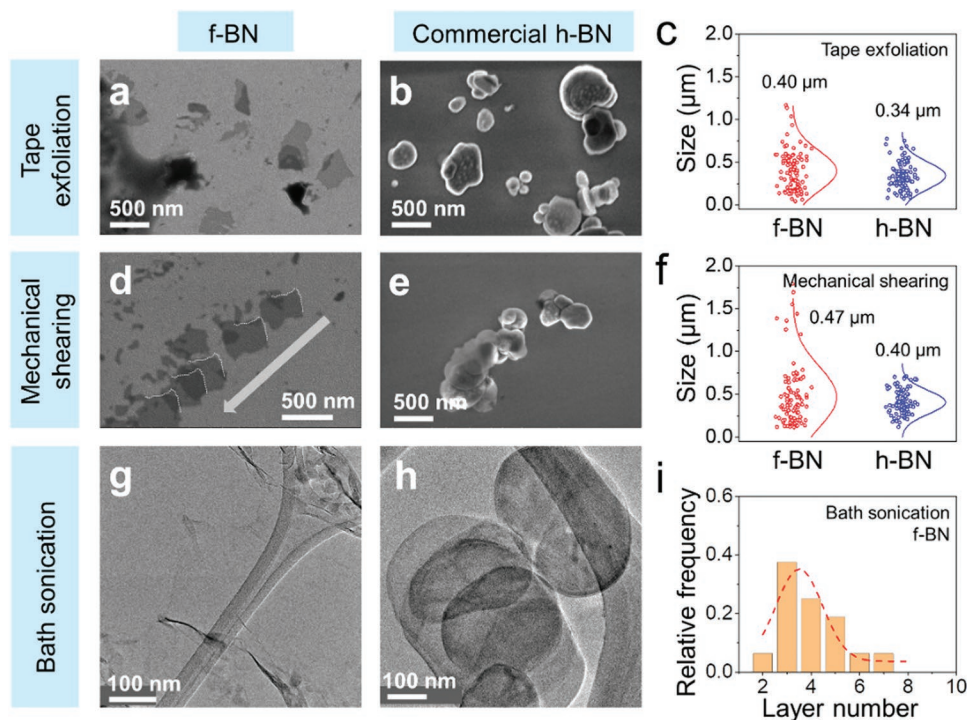
Figure 3. Mechanical exfoliation tests of f-BN. a,b) SEM images showing the tape exfoliation results of f-BN (a) and commercial h-BN (b). c) The size distributions of f-BN and commercial h-BN by the tape exfoliation method. Number of samples $N = 100$. d,e) SEM images showing the monodirectional mechanical shearing results of f-BN (d) and commercial h-BN (e). f) The size distributions of f-BN and commercial h-BN by the monodirectional mechanical shearing method. Number of samples, $N = 100$. g,h) TEM images of f-BN (g) and commercial h-BN (h) after bath sonication treatment, both atop a lacy carbon grid. i) The layer number distributions of the f-BN by the bath sonication treatment. Number of samples, $N = 16$.

demonstrated in the next section. The same exfoliation phenomena can be observed by applying monodirectional shearing force. The mechanical exfoliation of f-BN sheets is demonstrated in Figure 3d and Figure S20 (Supporting Information), representing exfoliated f-BN sheets with the same edge feature (delineated by the white dashed lines outlining each sheet). The direction of the monodirectional shearing force is shown by the white arrow in Figure 3d. The atomic force microscopy (AFM) profile (Figure S21, Supporting Information) shows the bilayer to few-layer features of the exfoliated f-BN sheets. These results indicate effective exfoliation of f-BN. In contrast, few-layer BN sheets cannot be directly prepared from commercial h-BN by monodirectional shearing under the same conditions (Figure 3e and Figure S22, Supporting Information). The average lateral size of f-BN and commercial h-BN, obtained from the mechanical shearing method, are 0.47 and 0.40 μm, respectively (Figure 3f). Compared to commercial h-BN nanoplates with >10 layers, few layer f-BN flakes of several hundred nanometers with ripple-like structures are obtained by bath sonication in ethanol without surfactant (Figure 3g,h). The layer number distributions of the f-BN, obtained by the bath sonication treatment show that ≈80% of the f-BN sheets have 3–5 layers (Figure 3i). In some regions, small black particles can be found, presumably from the carbon conductive additives. HRTEM images and corresponding FFT patterns demonstrate the high quality of the turbostratic f-BN sheets and the well-aligned structure of commercial h-BN nanoplates (Figure S23, Supporting Information).

2.4. Electrochemical Anticorrosion Tests of f-BN Composites

The turbostratic feature improves the dispersibility and stability of f-BN in aqueous solution (Figure S19, Supporting Information). After dispersal in aqueous Pluronic (F-127) (1 wt% in deionized water), the concentration of f-BN can reach up to ≈18 wt% higher than that of commercial h-BN. The percentage of commercial h-BN and f-BN still in solution are ≈6% and 77% after 21 d, respectively, which indicates the f-BN dispersion has a higher temporal stability. Good dispersibility of f-BN makes it possible to prepare stable nanocomposites with f-BN as a compatible additive. A prerequisite is the dispersion and distribution of the nanofillers inside polymer matrices, since strengthening of the composite relies on the interactions between the polymer and the surface area of the fillers.[1,41] PVA has been studied as a surface coating model system for testing additives to reduce chemical and electrochemical metal corrosion.[42,43] The barrier films provide tortuous diffusion pathways for corrosive electrolytes, delaying the metal corrosion process. Likewise, they prevent metal ions from migrating, thus building up a local Nernst potential at the polymer–metal interface. The addition of appropriate nanofillers can occupy the free volume within the polymer matrix and improve the film's blocking properties.[42] Since f-BN has shown good dispersibility in aqueous solution, further demonstrations of f-BN as fillers in PVA composites, which act as an electrochemical anticorrosion coating, are shown in **Figure 4**.

Before the electrochemical tests, the coating thickness was characterized by cross-sectional SEM images as shown in
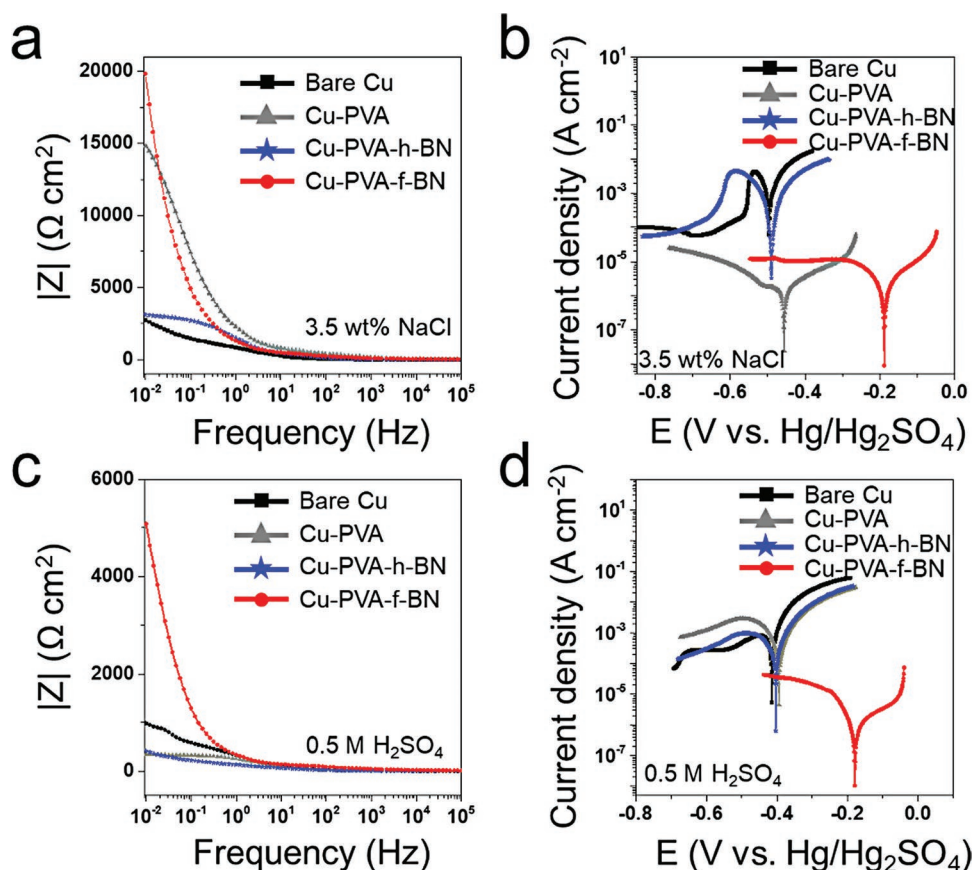
Figure 4. The electrochemical anticorrosion tests of f-BN composites. a,b) Electrochemical analysis of bare Cu, Cu-PVA, Cu-PVA-h-BN, and Cu-PVA-f-BN in 3.5 wt% NaCl (aq): a) Bode plots and b) Tafel plots. c,d) Electrochemical analysis of bare Cu, Cu-PVA, Cu-PVA-h-BN, and Cu-PVA-f-BN in 0.5 M H_2SO_4: c) Bode plots and d) Tafel plots.

Figure S24 (Supporting Information). The average thickness of the coating layer is ≈ 9 µm. The electrochemical linear polarization resistance (LPR) tests of bare Cu, PVA coated Cu (Cu-PVA), f-BN and PVA composite coated Cu (Cu-PVA-f-BN), and commercial h-BN and PVA composite coated Cu (Cu-PVA-h-BN) in 3.5 wt% saline solution are shown in Figure S25 (Supporting Information). The Cu-PVA-f-BN shows the largest polarization resistance (R_p) ≈22.8 kΩ cm², which is ≈47% higher than Cu-PVA. The open circuit potential (E_{corr}) represents the thermodynamic tendency of the electrode to lose electrons to the solution.[38,39] According to the Nernst equation, the metal surface remains relatively stable when the measured potential is lower than E_{corr}. The potentiodynamic polarization measurements in Figure 4a,b demonstrate that Cu-PVA-f-BN has the more positive E_{corr} (−188 mV vs Hg/Hg$_2$SO$_4$), thus there is less tendency for the surface metal to take part in the electrochemical oxidation process. Compared with pure PVA and PVA-h-BN composite coatings, the PVA-f-BN composite has higher corrosion protection efficiency (>92%) and better anticorrosion performance as shown in Table S5 (Supporting Information). The same enhanced anticorrosion trend is also observed in 0.5 M H_2SO_4 as shown in Figure 4c,d and Figure S26 (Supporting Information). The Cu-PVA-f-BN shows the largest polarization resistance (R_p) ≈10.0 kΩ cm², which is >20-fold higher than Cu-PVA. The corrosion protection efficiency for Cu-PVA-f-BN is

>97% versus 68% for Cu-PVA-h-BN as shown in Table S6 (Supporting Information). This likely harkens back to the superior dispersibility and compatibility of f-BN in the polymer matrix.

The optical and microscopic morphology after electrochemical testing indicates that the Cu under the PVA-f-BN composite coating is least affected (Figures S27–S29, Supporting Information), and surface elemental analyses (Figure S30, Supporting Information) also show there is no obvious formation of the oxides for Cu-PVA-f-BN. These results are consistent with the highest corrosion protection efficiency from the electrochemical tests and demonstrate one potential application of f-BN as a filler for nanocomposites.

Mechanical performance, such as hardness and Young's modulus of epoxy resin with 1 wt% f-BN additive shows ≈54% and ≈70% increase, respectively, compared to pure epoxy resin. These improvements cannot be achieved by replacing f-BN with equal amounts of commercial h-BN (Figure S31, Supporting Information).

2.5. Synthesis of f-BCN with Different Chemical Compositions

The atomic ratios of carbon can be tuned by directly changing the weight percent of carbon black in the reactants. If a mixture of BH_3NH_3 and 30 wt% carbon black is used as the reactant,

**ADVANCED
SCIENCE NEWS**

www.advancedsciencenews.com

**ADVANCED
MATERIALS**

www.advmat.de
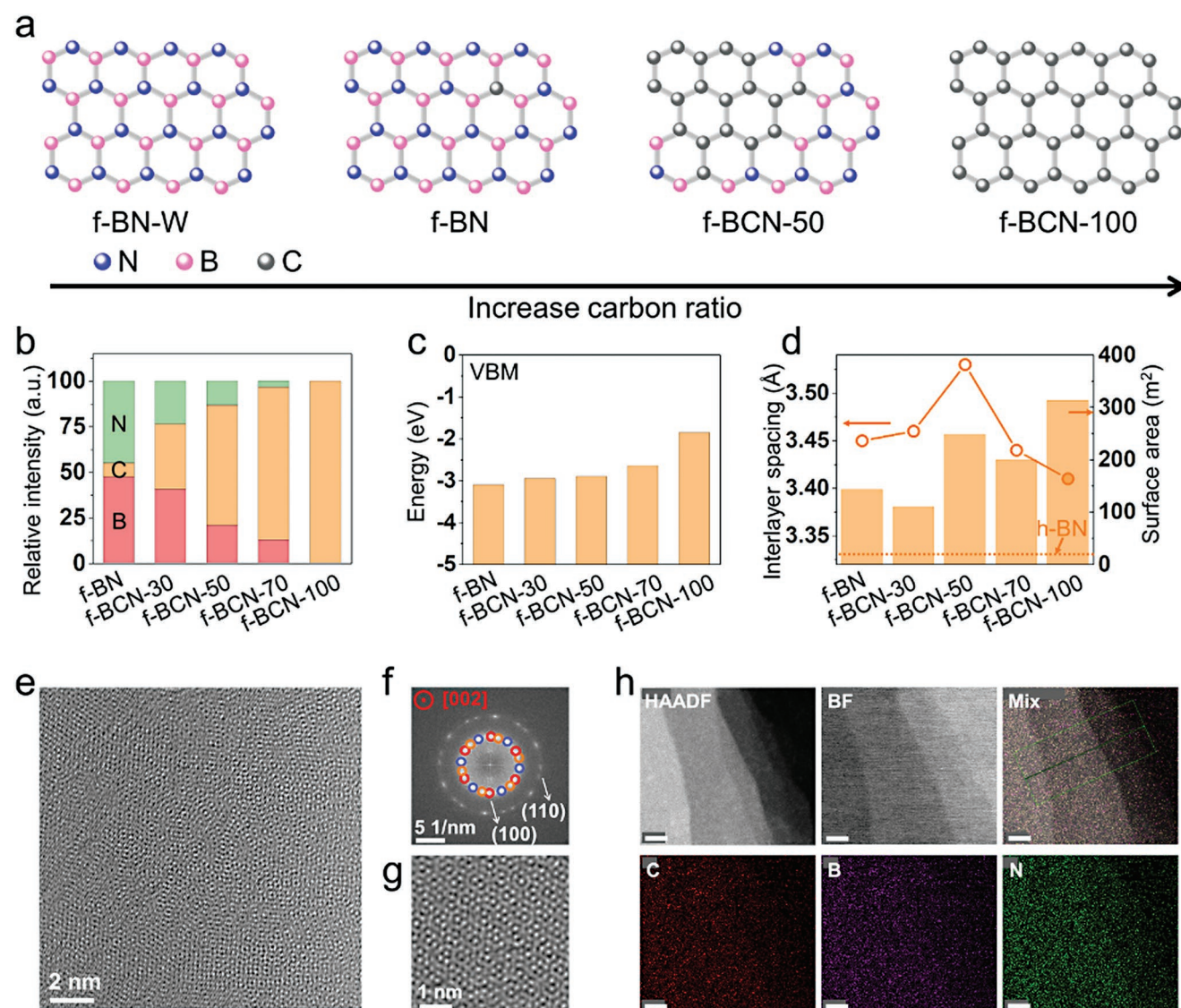
Figure 5. Characterizations of f-BCN with different chemical compositions. a) Schematic illustration of f-BCN with variable atomic ratios. b) The elemental distributions of different f-BCN samples. c) Valence band maximum of different f-BCN samples. d) Interlayer spacing and surface area of different f-BCN samples. e) TEM image of f-BCN-30 and f) corresponding FFT results. g) HRTEM image showing in-plane crystallinity of f-BCN-30. h) HAADF-STEM, BF-STEM images, and corresponding elemental distribution of f-BCN-30 sheets. Scale bars: 20 nm.

the flash product is called f-BCN-30. The same naming convention is used for the other f-BCN samples we prepared. As the weight percent of carbon increases, the atomic percentage of carbon in flash products can be controlled from ≈0% to ≈100% as determined by XPS results (**Figure 5**a). The elemental analyses demonstrate the monotonic decrease of B and N from f-BN to f-BCN-100 (Figure 5b). High-resolution XPS of C 1s spectra show the existence of C−B and C−N bonds in f-BCN samples. As the mass ratios of the carbon increase, the C−B and C−N ratios also increase (Figure S32, Supporting Information). High-resolution XPS of B 1s and N 1s spectra also confirm the existence of B−C and N−C bonds (Figure S33, Supporting Information). The presence of B−C and N−C bonds confirms the formation of in-plane hybrid structures instead of the out-of-plane stacked heterostructures, the latter being often more thermodynamically stable (Note S4,

Supporting Information).[37] This can be attributed to an ultrafast heating and cooling rate (≈10^4 K s^{-1}) of the FJH reaction as shown in Figure S34, Supporting Information. The presence of the conductive carbon materials can be seen from the TEM images (Figure S35, Supporting Information), which can cause the overestimation of the carbon ratios as determined by the XPS analysis. Due to the thermal stability difference of the conductive carbon materials and substitutional carbon species chemically bonded with boron and nitrogen, thermogravimetric analysis (TGA) is used to oxidize the conductive carbon materials (Figure S36, Supporting Information). The first-order derivative of the thermogravimetric curve (Figure S17c, Supporting Information) shows two peaks starting from ≈540 and ≈750 °C; the first peak is mainly attributed to the oxidation of conductive carbon materials. Therefore, the conductive carbon materials can be removed from the flash products by

controlling the temperature at ≈675 °C under air as shown in Figure S17d (Supporting Information). XPS results of various f-BCN samples before and after thermal treatment reflect the existence of the substitutional carbon species and the ratio of carbon content can reach 35.7 at% in f-BCN-70 after thermal treatment at ≈675 °C under air for 30 min (Figure S37, Supporting Information).

The carbon ratio of the in-plane hybrid structure affects the electronic structures and changes the VBM as shown in Figure S38 (Supporting Information). As the atomic ratios of carbon increase, the VBM of f-BCN changes from −3.10 to −1.85 eV (Figure 5c). The Raman spectra of different f-BCN samples (Figure S39, Supporting Information) show the appearance of the G peak (≈1580 cm^{-1}, single resonance), D peak (≈1350 cm^{-1}, intervalley double resonance), 2D peak (≈2695 cm^{-1}, second-order zone boundary phonons), D+G peak (≈2930 cm^{-1}, a combination of scattering peak), 2D′ (≈3250 cm^{-1}), and G* (≈2450 cm^{-1}).[44–46] As the carbon ratio increases in the reactants, the intensity of D+G peak decreases and 2D peak increases. The intensity ratio between D and G peaks for f-BCN-70 is ≈1.10, which is similar to boron and nitrogen co-doped graphene, which belongs to the carbon rich BCN. f-BCN-100 (FG) shows a high 2D to G ratio (≈8) and a low D peak, which is similar to previous work.[1] The introduction of carbon to the f-BCN sample also confers magnetic properties,[42] which is different from commercial h-BN (Figure S40, Supporting Information). h-BN shows a diamagnetic response since boron is bonded with nitrogen and the total magnetic moment is ≈0. However, f-BCN-50 has B−C/O and N−C/O bonds, which can contribute to the total magnetic moment. f-BCN-50 shows a ferrimagnetic response with a small coercivity of ≈22 Oe. The saturation magnetic moment of f-BCN-50 is 0.115 emu g^{-1}. Inductively coupled plasma mass spectrometry (ICP-MS) results (Figures S41 and S42 and Note S5, Supporting Information) confirm the negligible contribution from magnetic metals, such as Fe, Co, and Ni, and other d-block metals.[47,48]

The boron–carbon–nitrogen ternary phase diagram (Figure S43, Supporting Information) demonstrates the chemical compositions (boron, carbon, and nitrogen) of different f-BCN products before thermal treatments, showing broad accessibility to varied BCN materials via FJH methods. All of these f-BCN samples have turbostratic structures with larger interlayer spacings, since (002) diffraction peaks shift to lower angles with broad (10) peaks by XRD (Figure S44, Supporting Information). The interlayer spacing of f-BCN is 3%–6% larger than in commercial h-BN and f-BCN-50 has the largest interlayer spacing, which is ≈6.1% larger than in commercial h-BN (Figure 5d and Table S7, Supporting Information). There are larger surface areas for f-BCN samples (110–310 m^2 g^{-1}) and they have abundant micropores as well as mesopores (Figure 5d and Figure S45, Supporting Information). The Moiré patterns can be seen from the HRTEM image of f-BCN samples (Figure 5e), which indicates the existence of turbostratic stacking structure. Corresponding FFT patterns reflect multiple sets of the diffraction spots from [002] direction (Figure 5f). Atom-scale HRTEM image shows the complex Moiré patterns and good in-plane crystallinity (Figure 5g). STEM images confirm the nonaligned edges and elemental mapping results

demonstrate the existence of B, C, and N for f-BCN-30 samples (Figure 5h and Figure S46, Supporting Information). To confirm the existence of substitutional carbon species in the structure and exclude the possibility of hydrocarbon contamination resulting in false positive carbon signals, electron energy loss spectroscopy (EELS) is carried out (Figure S47, Supporting Information) and the C K-edge spectrum shows the existence of 1s-π* and 1s-σ* peaks, which indicates the existence of substitutional carbon atoms in the conjugated structure and excludes the possibility that the carbon signal is solely from amorphous hydrocarbon contamination.[49,50]

3. Conclusion

f-BCN with various chemical compositions and turbostratic characteristics can be synthesized from BH$_3$NH$_3$ and carbon black in <1 s using the ultrafast and solvent-free FJH method. The atomic percentage of carbon can be controlled from ≈0% to ≈100% and spectroscopic analyses show the VBM is correspondingly tuned. At the lower percentages of carbon, the f-BN is very close to t-BN in its spectroscopic characteristics. Theoretical calculations support the existence of turbostratic structures along with the energy barriers that impede conversion to the well-aligned counterparts. The obtained f-BCN layers with disordered orientation are easily exfoliated. Compared to commercial h-BN nanoplates, f-BCN samples demonstrate stable dispersibility in aqueous Pluronic (F-127, 1 wt% in deionized water). Furthermore, the addition of f-BCN as barrier fillers in PVA nanocomposites shows better compatibility and they confer higher corrosion protection efficiency. The turbostratic morphology of f-BCN is difficult to reproduce by common bottom-up methods, such as CVD and hydrothermal methods, whose cooling rates are 100–1000× lower than that of FJH. The FJH method offers a high-yield process to synthesize bulk quantities of turbostratic materials. Since the FJH process is being industrially scaled to ton per day levels, access to large quantities of f-BCN will likely be attainable using the same or similar equipment.[51]

4. Experimental Section

Materials: Commercial h-BN (11078-50G, 99.5% metal basis) was purchased from Johnson Matthey Company. Borane ammonia complex (682098-10G, 97%) was purchased from Millipore-Sigma. PVA (341584-500G, average Mw 89 000–98 000, 99+% hydrolyzed) was purchased from Millipore-Sigma. Cu foil (0.025 mm, annealed, uncoated, 99.8% metal basis) was purchased from Alfa Aesar. Carbon black (APS 10 nm, Black Pearls 2000) was purchased from Cabot Corporation. DER 736 (Lot No. BCBM6627V) was obtained from Millipore-Sigma and used as received. 1,5-Diamino-2-methylpentane (Dytek A, Lot No. SHBG9920V) was obtained from Millipore-Sigma and used as received.

FJH System: The FJH system has been described in previous publications.[1] The circuit diagram and FJH reaction box are shown in Figure S1 (Supporting Information). Ar gas (≈1 atm) was used as an inert atmosphere to avoid sample oxidation during the FJH reaction. The mixed reactant was composed of BH$_3$NH$_3$ and conductive additives. The conductive carbon additives can be carbon black and metal powders, such as tungsten and iron. The reactant powder was ground and mixed homogeneously using a mortar and pestle for ≈10 min before being loaded into the reaction tube. Here, the reaction tube can be a quartz or

Table 1. Flash parameters for different systems.

	f-BN (f-BCN-20)	f-BCN-30	f-BCN-50	f-BCN-70
Reactant	BH_3NH_3 + CB (20 wt%)	BH_3NH_3 + CB (30 wt%)	BH_3NH_3 + CB (50 wt%)	BH_3NH_3 + CB (70 wt%)
Sample mass [mg]	60	50	50	50
Sample resistance [Ω]	≈40	≈18	≈2.0	≈1.0
Discharge voltage [V]	150	120	120	120
Flash duration [ms]	600	500	200	200
Flash repetitions	1 flash	1 flash	1 flash	1 flash
Total capacitance [mF]	60	60	60	60
Chamber pressure [atm Ar]	1	1	1	1
	FG (f-BCN-100)	f-BN-W	f-BN-Fe	
Reactant	CB	BH_3NH_3 + W (95 wt%)	BH_3NH_3 + Fe (90 wt%)	
Sample mass [mg]	30	840	400	
Sample resistance [Ω]	≈0.7	≈50	≈400	
Discharge voltage [V]	110	80	60	
Flash duration [ms]	100	500	500	
Flash repetitions	1 flash	1 flash	1 flash	
Total capacitance [mF]	60	60	60	
Chamber pressure [atm Ar]	1	1	1	

ceramic. The mass loading in the 4-mm tube was no more than 60 mg. Generally, graphite spacers are not recommended in this reaction since a large amount of gas is expelled from the reaction tube, which can cause the tube explosion or flash jig damage. Unless specified, copper wool plugs were used as electrodes to slightly compress the loaded powder while permitting outgassing.

For f-BCN-20, the compressing force was controlled by a small vise connected to a rotary knob as shown in Figure S1b (Supporting Information), to tune the sample resistance to ≈150 Ω. The Arduino controller relay with programmable millisecond-level delay time was used to control the discharge time and the electric energy was provided by a capacitor bank with a total capacitance of 60 mF. The capacitor bank was charged by a DC power supply capable of reaching 400 V. A pretreatment with discharge voltage 200 V and discharge time 200 ms was necessary for degassing and subsequent homogenous FJH reaction. The resistance after the pretreatment was ≈40 Ω. The FJH reaction was carried out with 150 V and optimized duration of 600 ms. After the FJH reaction, the apparatus was allowed to cool and vent for 3 min. The f-BCN-20 was called f-BN in this context since it had similar spectroscopic features as h-BN (Figure 2). For a quartz tube with 4 mm diameter and 5 cm length, the optimized sample weight was 60 mg. For other f-BCN samples, the parameters are listed in **Table 1**. Additional safety notes can be seen in the Supplemental text.

Characterization: A Thermo Scientific Nicolet 6700 attenuated total reflectance Fourier transform infrared (ATR-FTIR) spectrometer (Waltham, MA, USA) was used to analyze the vibration and rotation modes in the reactant and the flash product. Raman spectra were collected with a Renishaw Raman microscope using a 532-nm laser with a power of ≈1 mW to avoid the heating effect and sample damage. A 50× lens was used for local Raman spectra. For high resolution Raman spectra, an exposure time of 1 s with integration time 300 times was used. XRD measurements were done by a Rigaku SmartLab Intelligent XRD system with filtered Cu Kα radiation (λ = 1.5406 Å). BET characterization was done on a Quantachrome Autosorb-iQ3-MP/Kr BET surface analyzer. UV–vis absorption spectra were obtained on a SHIMADZU UV-3600Plus configured with a photomultiplier tube from 190 to 800 nm wavelength. XPS spectrograms were collected with a PHI Quantera SXM Scanning X-ray Microprobe with a base pressure of 5×10^{-9} Torr. Survey spectra were recorded using 0.5 eV step sizes with a pass energy of 140 eV. Elemental spectra were recorded using 0.1 eV step sizes with a pass energy of 26 eV. All the XPS spectra were corrected using the C 1s peaks (284.8 eV) as reference. The mechanically exfoliated samples on Si wafers were analyzed through SEM using a FEI Helios Nano Lab 660 Dual Beam SEM at 5 kV and 25 pA with a working distance of 4 mm. To increase the conductivity and contrast, the Si wafer was coated with ≈15 nm Au by sputtering prior to shearing. TEM images were taken with a JEOL 2100F field emission gun TEM at 200 kV. HRTEM and HAADF-STEM images and corresponding elemental analyses were taken with FEI Titan Themis S/TEM instrument at 300 kV after accurate spherical aberration correction. AFM results were collected using a Park NX20 AFM system in non-contact mode. TGA and differential scanning calorimetry (DSC) data were collected from 25 to 1000 °C under air. The heating rate was set to 10 °C min⁻¹. The air flow was maintained at 80 mL min⁻¹ throughout the run.

Mechanical Exfoliation: Three different methods were used to mechanically exfoliate the commercial h-BN and f-BN. The first was to apply a monodirectional shearing force. The sample was sandwiched between two Si wafers that were coated with ≈15 nm Au. The ≈15 nm Au coating was formed by sputtering for ≈10 min. A monodirectional shearing force was applied once to exfoliate the sample flakes. The second method was clear adhesive tape exfoliation. A Si wafer was cleaned with acetone, ethanol, and deionized water in sequence (5 min each). Then an oxygen plasma was used to treat the clean Si wafer (8 min) before use. The treated Si wafer was placed on a heating plate (110 °C). Clear adhesive tape was used to exfoliate the powder sample ≈20 times. Subsequently, the tape with sample was applied on a Si wafer, and the temperature was maintained at 110 °C for 90 s. Finally, the tape was carefully removed, and the Si wafer was used for microscopic analysis. The third exfoliation method was by bath sonication. A Cole-Parmer 8891 ultrasonic machine was used. The powder sample was sonicated in ethanol for ≈10 min before it was dropped on a Cu grid to be followed by microscopic analysis.

Dispersion Test: The f-BN (2–8 mg mL⁻¹) was added to aqueous Pluronic (F-127, 1 wt% in deionized water). The mixture was bath sonicated for 30 min to obtain the dispersion by bath sonicator (Cole-Parmer 8891). The supernatant was analyzed by UV–vis spectroscopy. The dispersions were diluted 100 times and the absorbance was recorded at 300 nm. An extinction coefficient of α_{300} = 3177 L g⁻¹ m⁻¹ was used to calculate the concentration of BN in the aqueous solution.[52]

**ADVANCED
SCIENCE NEWS**

www.advancedsciencenews.com

**ADVANCED
MATERIALS**

www.advmat.de

Anticorrosion Test: PVA (0.5 g) was mixed with deionized water (10 mL), followed by stirring the mixture at 50 °C for 30 min. The mixture was then bath sonicated for 10 min at room temperature to form a thick clear solution. The commercial h-BN or f-BN (0.05 g) was added to the solution and the mixture was sonicated for another 30 min. The final solution was painted with a brush on a clean Cu foil that had been washed by ethanol and deionized water in sequence. The coated Cu was allowed to air dry at room temperature. The final thickness of the BN/PVA composite was determined by cross-sectional SEM images.

Electrochemical measurements were carried out in a three-electrode configuration using a CHI 608D electrochemical workstation. A graphite rod and Hg/Hg_2SO_4, K_2SO_4 (saturated) electrode were used as the counter and reference electrodes, respectively. The electrochemical tests were carried out after the stable open circuit potential (OCP) was recorded. The electrolytes used included 0.5 M sulfuric acid and 3.5 wt% saline solution. Electrochemical impedance spectroscopy was measured at room temperature between 100 kHz and 0.01 Hz with an amplitude of 5 mV. Nondestructive linear polarization resistance (LPR) tests were run to calculate corrosion rates by polarizing the working electrode at ±10 mV from its OCP and using a scan rate of 0.1 mV s^{-1}. Tafel analysis was used to calculate the Tafel constants with a scan rate of 1 mV s^{-1} in the potential range of ±250 mV (vs OCP). The electrochemical tests were run three times. After the electrochemical test, the surface coating was removed, and the surface of the Cu was characterized by SEM. For comparison, bare Cu and PVA-coated Cu foil were tested using the same method, and the samples with commercial h-BN and f-BN were called Cu–PVA-h-BN and Cu-PVA-f-BN, respectively.

Electrochemical Calculation: The polarized resistance (R_p) was determined by the slope of the I–V curve as shown in Figures S25 and S26 (Supporting Information). The corrosion current (i_{corr}) was calculated by using the Stern–Geary Equation (1)[12,42]

$$i_{corr} = \frac{\beta_a \beta_c}{\beta_a + \beta_c} \times \frac{1}{2.3 R_P} \tag{1}$$

β_a and β_c refer to the anodic and cathodic Tafel constants, respectively, which are calculated based on the electrochemical analysis as shown in Figure 4b,d.

Corrosion potential (E_{corr}) was determined by the potential at the lowest current density based on Tafel analysis. The corrosion rate (mils per year (mpy), where 1 mil = 0.0254 mm) was calculated using Equation (2)[12]

$$\text{Corrosion rate} = \frac{K i_{corr}(EW)}{\rho A} \tag{2}$$

The *EW* and ρ refer to the equivalent weight (31.7 g) and density (8.94 g cm^{-3}) of the Cu specimen, respectively. *A* is the surface area (≈1 cm^2) in the electrochemical test. When the i_{corr} uses µA cm^{-2} as the unit, the constant K = 0.1288 is needed to convert the unit of corrosion rate into mpy.

The corrosion protection efficiency could be further calculated using Equation (3)[42]

$$\text{Corrosion protection efficiency} = \frac{(i_{corr}^0 - i_{corr})}{i_{corr}^0} \times 100\% \tag{3}$$

Mechanical Test for Composites: DER 736 (3 g) was combined with 1,5-diamino-2-methylpentane curing agent (0.45 g) in a 20 mL scintillation vial, along with either f-BN or commercial h-BN (30 mg). The solution was then stirred at room temperature with a magnetic stir bar for 30 min at 300 rpm. The solution was transferred to a cup-horn sonicator and sonicated for 15 min at 50% amplitude before being high shear mixed for 15 min at ≈10 000 rpm. After degassing within a vacuum dessicator for 1 h, the solution was cured for 2 h at 70 °C, then at room temperature overnight. The scintillation vial was then broken to release the composite and sanded using the face of an abrasive wheel, then 800, 1000, 1200, and 2500 grit sandpaper to the appropriate dimensions for microscale mechanical testing. Manual wet sanding was carried out by slightly wetting the sandpaper before transitioning to the next higher grit of sandpaper.

Nanoindentation was carried out using a Hysitron TI 980 Triboindenter equipped with a diamond Berkovich tip with a pyramidal geometry. To calculate the indentation modulus and hardness, at least five different indentations were performed for each sample with a maximum displacement of 500 nm and a displacement rate of 10 nm s^{-1}. Elastic modulus and hardness were calculated using the Oliver–Pharr approach, using the equations below[1]

$$E_r = \frac{\sqrt{\pi}}{2} \times \frac{S}{\sqrt{Ap}} \tag{4}$$

$$\frac{1}{E_r} = \frac{1-\nu^2}{E} + \frac{1-\nu_i^2}{E_i} \tag{5}$$

$$H = \frac{P}{Ap} \tag{6}$$

where E_r is the reduced elastic modulus; *S* is the stiffness of the initial part of the unloading curve; *Ap* is the projected area of contact; E and v are the elastic modulus and Poisson's ratio of the sample, respectively; E_i and ν_i are the elastic modulus and Poisson's ratio of the indenter, respectively; *H* is the hardness; and *P* is the applied load.

Nudged Elastic Band Simulation: The NEB simulations were carried out using Large-scale Atomic/Molecular Massively Parallel Simulator (LAMMPS).[53] All-atom Lennard-Jones and electrostatic interactions were used to model the interlayer and intralayer interaction energies between h-BN layers.[54]

Finite Element Simulation: Initial processing of data was performed in Wolfram Mathematica 11.3.[55] Five current versus time curves recorded at 20 kHz were averaged, to obtain a representative current profile for the flash process. To remove measurement noise, a median filter of ten adjacent datapoints was applied. Subsequently, the data were fit with a sixth-order polynomial with no t^0 term. The removal of the constant term forces the current to be 0 A at t = 0 s, thereby eliminating the small amount of fictitious current before the beginning of the flash that originates from measurement noise. The sixth-order polynomial fit captured the overall shape features of the current profile, and as compared to a 50th order polynomial fit, the total amount of charge represented by the sixth-order polynomial approximation to the current was within 0.3% of the measured charge.

The model was built using COMSOL Multiphysics 5.5.[56] The porosity of the copper wool electrodes was accounted for by multiplying the heat capacity, thermal conductivity, density, and electrical conductivity of copper by 0.2, which represents the approximate packing density. The voltage was applied through a terminal, and the potential at the end of the opposite electrode was grounded at V = 0. The thermal conductivity of the f-BN[57] was approximated using data extracted using WebPlotDigitize from a classic study on the temperature-dependent thermal conductivity of hexagonal boron nitride, and corrections for packing density along with the thermal conductivity of the electrically conductive carbon additive[58] were performed using a weighted average. The temperature-dependent heat capacity was approximated using a Reshetnikov's equation.[59]

Statistical Analysis: The electrochemical data were used without any preprocessing. The XPS data, FTIR results, Raman results, and XRD results were normalized based on the maximum intensity of the spectra for the purpose of presentation. The Raman results reflect the statistical analyses, in which the Raman shifts shows the E_{2g} peak from 100 sampling points, respectively. The size distributions of f-BN samples were calculated from 100 sheets. The layer number distributions of f-BN samples were calculated from 16 samples.

Supporting Information

Supporting Information is available from the Wiley Online Library or from the author.

Conflict of Interest

Rice University owns intellectual property on the formation of boron nitride and other 2-dimensional materials by flash Joule heating. That intellectual property has been licensed to a company in which J.M.T. is a stockholder. But he is not an officer, director, or employee of that company. Conflicts of interest are mitigated through regular disclosure to and compliance with the Rice University Office of Sponsored Programs and Research Compliance. The authors declare no other conflicts.

Author Contributions

W.C. conducted the synthesis and characterizations with the help of C.G. and J.C. The mechanical exfoliation tests were done by W.C., C.G., and J.T.L. STEM and EDS were conducted by J.T.L., G.G., C.H.C., Y.H., and Z.W. W.A.A. helped with the dispersion tests. AFM was conducted by P.A.A. TGA was assisted by E.A.M. BET and XRD were conducted by K.M.W. and W.C. D.X.L. designed the flash Joule heating system. K.L. did the DRS tests. Z.Y. did the theoretical calculations and simulation analysis. W.C. and J.M.T. wrote the manuscript. All aspects of the research were overseen by J.M.T. All authors discussed the results and commented on the manuscript.

Data Availability Statement

The data that support the findings of this study are available from the corresponding author upon reasonable request within a reasonable amount of time after publication.

[1] D. X. Luong, K. V. Bets, W. A. Algozeeb, M. G. Stanford, C. Kittrell, W. Chen, R. V. Salvatierra, M. Ren, E. A. McHugh, P. A. Advincula, Z. Wang, M. Bhatt, H. Guo, V. Mancevski, R. Shahsavari, B. I. Yakobson, J. M. Tour, *Nature* **2020**, *577*, 647.

[2] M. G. Stanford, K. V. Bets, D. X. Luong, P. A. Advincula, W. Y. Chen, J. T. Li, Z. Wang, E. A. McHugh, W. A. Algozeeb, B. I. Yakobson, J. M. Tour, *ACS Nano* **2020**, *14*, 13691.

[3] R. J. Smith, P. J. King, M. Lotya, C. Wirtz, U. Khan, S. De, A. O'Neill, G. S. Duesberg, J. C. Grunlan, G. Moriarty, J. Chen, J. Wang, A. I. Minett, V. Nicolosi, J. N. Coleman, *Adv. Mater.* **2011**, *23*, 3944.

[4] P. A. Advincula, D. X. Luong, W. Y. Chen, S. Raghuraman, R. Shahsavari, J. M. Tour, *Carbon* **2021**, *178*, 649.

[5] W. A. Algozeeb, P. E. Savas, D. X. Luong, W. Chen, C. Kittrell, M. Bhat, R. Shahsavari, J. M. Tour, *ACS Nano* **2020**, *14*, 15595.

[6] K. M. Wyss, J. L. Beckham, W. Chen, D. X. Luong, P. Hundi, S. Raghuraman, R. Shahsavari, J. M. Tour, *Carbon* **2021**, *174*, 430.

[7] W. Chen, Z. Wang, K. V. Bets, D. X. Luong, M. Ren, M. G. Stanford, E. A. McHugh, W. A. Algozeeb, H. Guo, G. Gao, B. Deng, J. Chen, J. T. Li, W. T. Carsten, B. I. Yakobson, J. M. Tour, *ACS Nano* **2021**, *15*, 1282.

[8] K. Ba, W. Jiang, J. Cheng, J. Bao, N. Xuan, Y. Sun, B. Liu, A. Xie, S. Wu, Z. Sun, *Sci. Rep.* **2017**, *7*, 45584.

[9] L. Song, L. J. Ci, H. Lu, P. B. Sorokin, C. H. Jin, J. Ni, A. G. Kvashnin, D. G. Kvashnin, J. Lou, B. I. Yakobson, P. M. Ajayan, *Nano Lett.* **2010**, *10*, 3209.

[10] D. Xu, W. Y. Chen, M. Q. Zeng, H. F. Xue, Y. X. Chen, X. H. Sang, Y. Xiao, T. Zhang, R. R. Unocic, K. Xiao, L. Fu, *Angew. Chem., Int. Ed.* **2018**, *57*, 755.

[11] H. Rydberg, M. Dion, N. Jacobson, E. Schroder, P. Hyldgaard, S. I. Simak, D. C. Langreth, B. I. Lundqvist, *Phys. Rev. Lett.* **2003**, *91*, 126402.

[12] G. Chilkoor, K. Jawaharraj, B. Vemuri, A. Kutana, M. Tripathi, D. Kota, T. Arif, T. Filleter, A. B. Dalton, B. I. Yakobson, M. Meyyappan, M. M. Rahman, P. M. Ajayan, V. Gadhamshetty, *ACS Nano* **2020**, *14*, 14809.

[13] C. X. Wang, J. L. Zuo, L. F. Tan, M. Q. Zeng, Q. Q. Zhang, H. N. Xia, W. H. Zhang, Y. S. Fu, L. Fu, *J. Am. Chem. Soc.* **2017**, *139*, 13997.

[14] M. Kakiagea, D. Yoshikoshi, I. Yanase, H. Kobayashi, *Key Eng. Mater.* **2013**, *534*, 55.

[15] J. Ahn, S. F. Yoon, Q. Zhang, J. Cui, M. B. Yu, *J. Appl. Phys.* **2000**, *87*, 4022.

[16] J. B. Lian, T. Kim, X. D. Liu, J. M. Ma, W. J. Zheng, *J. Phys. Chem. C* **2009**, *113*, 9135.

[17] C. C. Cao, J. W. Yang, S. Yan, W. J. Bai, Y. H. Ma, Y. M. Xue, C. C. Tang, *2D Mater.* **2022**, *9*, 015014.

[18] U. B. Demirci, *Energies* **2020**, *13*, 3071.

[19] G. Puyoo, F. Teyssandier, R. Pailler, C. Labrugere, G. Chollon, *Carbon* **2017**, *122*, 19.

[20] B. Zhong, X. D. Zhang, L. Xia, Y. L. Yu, G. W. Wen, *Mater. Des.* **2017**, *120*, 266.

[21] W. Y. Chen, C. Ge, J. T. Li, J. L. Beckham, Z. Yuan, K. M. Wyss, P. A. Advincula, L. Eddy, C. Kittrell, J. H. Chen, D. X. Luong, R. A. Carter, J. M. Tour, *ACS Nano* **2022**, *16*, 6646.

[22] W. Y. Chen, J. T. Li, Z. Wang, W. A. Algozeeb, D. X. Luong, C. Kittrell, E. A. McHugh, P. A. Advincula, K. M. Wyss, J. L. Beckham, M. G. Stanford, B. Jiang, J. M. Tour, *ACS Nano* **2021**, *15*, 11158.

[23] Y. G. Yao, Z. N. Huang, P. F. Xie, S. D. Lacey, R. J. Jacob, H. Xie, F. J. Chen, A. M. Nie, T. C. Pu, M. Rehwoldt, D. W. Yu, M. R. Zachariah, C. Wang, R. Shahbazian-Yassar, J. Li, L. B. Hu, *Science* **2018**, *359*, 1489.

[24] T. Li, A. D. Pickel, Y. G. Yao, Y. N. Chen, Y. Q. Zeng, S. D. Lacey, Y. J. Li, Y. L. Wang, J. Q. Dai, Y. B. Wang, B. Yang, M. S. Fuhrer, A. Marconnet, C. Dames, D. H. Drew, L. B. Hu, *Nat. Energy* **2018**, *3*, 148.

[25] J. L. Beckham, K. M. Wyss, Y. Xie, E. A. McHugh, J. T. Li, P. A. Advincula, W. Y. Chen, J. Lin, J. M. Tour, *Adv. Mater.* **2022**, *34*, 2106506.

[26] S. Frueh, R. Kellett, C. Mallery, T. Molter, W. S. Willis, C. King'ondu, S. L. Suib, *Inorg. Chem.* **2011**, *50*, 783.

[27] L. F. Tan, J. L. Han, R. G. Mendes, M. H. Rümmeli, J. X. Liu, Q. Wu, X. Y. Leng, T. Zhang, M. Q. Zeng, L. Fu, *Adv. Electron. Mater.* **2015**, *1*, 1500223.

[28] Y. Ding, M. Zeng, Q. Zheng, J. Zhang, D. Xu, W. Chen, C. Wang, S. Chen, Y. Xie, Y. Ding, S. Zheng, J. Zhao, P. Gao, L. Fu, *Nat. Commun.* **2021**, *12*, 5886.

[29] W. Ding, L. Hu, J. Dai, X. Tang, R. Wei, Z. Sheng, C. Liang, D. Shao, W. Song, Q. Liu, M. Chen, X. Zhu, S. Chou, X. Zhu, Q. Chen, Y. Sun, S. X. Dou, *ACS Nano* **2019**, *13*, 1694.

[30] B. J. Zou, X. J. Chang, J. X. Yang, S. C. Wang, J. L. Xu, S. R. Wang, S. Samukawa, L. D. Wang, *Prog. Org. Coat.* **2019**, *133*, 139.

[31] R. V. Gorbachev, I. Riaz, R. R. Nair, R. Jalil, L. Britnell, B. D. Belle, E. W. Hill, K. S. Novoselov, K. Watanabe, T. Taniguchi, A. K. Geim, P. Blake, *Small* **2011**, *7*, 465.

[32] Q. R. Cai, D. Scullion, A. Falin, K. Watanabe, T. Taniguchi, Y. Chen, E. J. G. Santos, L. H. Li, *Nanoscale* **2017**, *9*, 3059.

[33] S. Alkoy, C. Toy, T. Gönül, A. Tekin, *J. Eur. Ceram. Soc.* **1997**, *17*, 1415.

[34] J. Thomas, N. E. Weston, T. E. O'Connor, *J. Am. Chem. Soc.* **1963**, *84*, 4619.

[35] I. S. Gladkaya, G. N. Kremkova, V. N. Slesarev, *J. Alloys Compd.* **1986**, *117*, 241.

[36] S.-Q. Hu, Y. Wang, L.-L. Liu, *J. Chem.* **2019**, *2019*, 8793282.

[37] L. J. Ci, L. Song, C. H. Jin, D. Jariwala, D. X. Wu, Y. J. Li, A. Srivastava, Z. F. Wang, K. Storr, L. Balicas, F. Liu, P. M. Ajayan, *Nat. Mater.* **2010**, *9*, 430.

[38] J. H. Warner, M. H. Rummeli, T. Gemming, B. Buchner, G. A. D. Briggs, *Nano Lett.* **2009**, *9*, 102.

[39] L. H. Li, J. Cervenka, K. Watanabe, T. Taniguchi, Y. Chen, *ACS Nano* **2014**, *8*, 1457.

[40] S. Gupta, R. Sachan, J. Narayan, *ACS Appl. Nano Mater.* **2020**, *3*, 7930.

[41] F. T. Alabdullah, *Ph.D. Thesis*, Colorado School of Mines, Golden, CO, USA **2018**.

[42] N. Sarkar, G. Sahoo, R. Das, G. Prusty, D. Sahu, S. K. Swain, *Ind. Eng. Chem. Res.* **2016**, *55*, 2921.

[43] P. S. Owuor, O.-K. Park, C. F. Woellner, A. S. Jalilov, S. Susarla, J. Joyner, S. Ozden, L. X. Duy, R. V. Salvatierra, R. Vajtai, J. M. Tour, J. Lou, D. S. Galvão, C. S. Tiwary, P. M. Ajayan, *ACS Nano* **2017**, *11*, 8944.

[44] L. Huang, S. Xu, Z. Wang, K. Xue, J. Su, Y. Song, S. Chen, C. Zhu, B. Z. Tang, R. Ye, *ACS Nano* **2020**, *14*, 12045.

[45] J. Hong, M. K. Park, E. J. Lee, D. Lee, D. S. Hwang, S. Ryu, *Sci. Rep.* **2013**, *3*, 2700.

[46] D. Yoon, H. Cheong, *Raman Spectroscopy for Characterization of Graphene*, Springer-Verlag, Berlin, Germany **2012**.

[47] M. M. Fan, J. J. Wu, J. T. Yuan, L. Z. Deng, N. Zhong, L. He, J. W. Cui, Z. X. Wang, S. K. Behera, C. H. Zhang, J. W. Lai, B. I. Jawdat, R. Vajtai, P. Deb, Y. Huang, J. S. Qian, J. Z. Yang, J. M. Tour, J. Lou, C.-W. Chu, D. P. Sun, P. M. Ajayan, *Adv. Mater.* **2019**, *31*, 1805778.

[48] C. Zhao, Z. Xu, H. Wang, J. Wei, W. Wang, X. Bai, E. Wang, *Adv. Funct. Mater.* **2014**, *24*, 5985.

[49] F. Langenhorsta, V. L. Solozhenko, *Phys. Chem. Chem. Phys.* **2002**, *4*, 5183.

[50] C. M. McGilvery, A. E. Goode, M. S. P. Shaffer, D. W. McComb, *Micron* **2012**, *43*, 450.

[51] Graphene in a flash, https://www.universalmatter.com/ (accessed: January 2022).

[52] M. M. Zhu, G. H. Li, X. M. Zhang, J. X. Zhai, S. P. Gan, X. Sond, *J. Inorg. Mater.* **2019**, *34*, 817.

[53] S. Plimpton, *J. Comput. Phys.* **1995**, *117*, 1.

[54] A. G. Rajan, M. S. Strano, D. Blankschtein, *J. Phys. Chem. Lett.* **2018**, *9*, 1584.

[55] Mathematica, Version 11.3, Wolfram Research, Inc., Champaign, IL, USA, **2018**.

[56] COMSOL Multiphysics® v. 5.5, https://www.comsol.com/ (accessed: July 2021).

[57] A. Simpson, A. D. Stuckes, *J. Phys. C: Solid State Phys.* **1971**, *4*, 1710.

[58] M. E. Spahr, R. Gilardi, D. Bonacchi, *Fillers for Polymer Applications*, Springer, Cham, Switzerland **2017**, p. 375.

[59] *Properties of Group III Nitrides* (Ed: J. H. Edgar), INSPEC, Institution of Electrical Engineers, London, UK **1994**.